Measured buffeting response of a long-span suspension bridge compared with numerical predictions based on design wind spectra

Aksel Fenerci*, Ph.D. candidate, Department of Structural Engineering, Norwegian University of Science and Technology, Trondheim, Norway

Ole Øiseth, Ph.D., Department of Structural Engineering, Norwegian University of Science and Technology, Trondheim, Norway

Keywords: long-span bridge, wind-induced vibration, buffeting theory, long-term monitoring, field measurement, turbulence characteristics

Abstract

Wind-induced vibrations of the Hardanger Bridge deck were studied with reference to turbulence characteristics at the bridge site to evaluate the performance of the state-of-the-art methods for buffeting response analysis. Long-term monitoring data from an extensive monitoring system were used to obtain the bridge vibrations and wind characteristics. The acceleration response of the bridge was calculated in the frequency domain using multimode buffeting theory. Design regulations were used directly and also modified using measurement data to deduce the wind turbulence spectra. The aerodynamic properties of the bridge section obtained from previous wind tunnel tests were used in the analyses. The predicted root mean square (RMS) acceleration response was compared to the measured response. The analysis using the design methodology gave underestimations of the measured responses. The use of average values of wind statistics obtained from the monitoring data only slightly improved the results. When the variability of the wind field was reflected into the design method by using the probability distributions of the wind field parameters, more satisfactory design curves were obtained.

1. Introduction

Along the western coast of Norway, Coastal Highway E39 connects Trondheim to Kristiansand. This highway is of vital importance to the Norwegian economy, as the majority of the country's exports are transported along this coastline. However, due to the unique topography of the Norwegian fjords, eight

* Corresponding author: aksel.fenerci@ntnu.no

ferries currently operate on this highway, resulting in increased travel time. Recently, the Norwegian Public Roads Administration (NPRA) has initiated an effort to replace the ferry connections with road transportation. The straits to be crossed vary in width from 1.5 km to 4 km (Nordfjorden, 1.5 km; Halsafjorden, 2 km; Sulafjorden, 3.8 km; and Sognefjorden, 3.7), and the seabed in these areas is generally very deep (600 – 1500 meters). For most of the crossings, suspension bridges are considered to be the primary option, which would require designing and constructing suspension bridges with unmatched scale in a complex, wind-prone terrain. Experience suggests that wind effects on slender structures such as these can be critical and even destructive; therefore, accurately predicting the wind-induced dynamic response is essential for reliable design (Larsen and Larose 2015; Miyata 2003).

In wind resistant design of long-span suspension bridges, predicting the buffeting response is one of the most important steps, particularly for the serviceability and fatigue limit states (Simiu and Scanlan 1996; Xu 2013). First formulized by Davenport (1962), the stochastic theory for buffeting response analysis was later improved by Scanlan and Tomko (1971) the introduction of aerodynamic derivatives for describing the self-excited forces. Recently, a multimode approach has been adopted by many researchers. This analysis can be conducted either in frequency domain (Chen et al. 2001; Jain et al. 1996; Øiseth et al. 2010; Scanlan 1978; Zhu and Xu 2005) or time domain (Caracoglia and Jones 2003; Chen et al. 2000; Chen and Kareem 2001; Costa et al. 2007; Øiseth et al. 2012).

In recent years, structural health monitoring (SHM) systems have been installed on many long-span cable-supported bridges around the world (Brownjohn et al. 1994; Caetano et al. 2015; Cross et al. 2013; Hui et al. 2009; Macdonald 2003; Miyata et al. 2002; Wang et al. 2011, 2013) to ensure safety and to monitor the structural behavior of these large and complex structures. The environmental and structural data obtained from these measurements have been used extensively by researchers in several applications, e.g., to establish wind characteristics, to study and predict the dynamic response or to calibrate finite element (FE) models. However, the number of studies where the measured response was compared to analytical predictions are rather limited. Bietry et al. (1995) compared the acceleration response of a suspension bridge with analytical predictions and reported that using quasi-steady theory and aerodynamic admittance functions set to unity led to conservative predictions. Macdonald (2003) used quasi-steady theory and Davenport’s original formulation to calculate the wind-induced response of the Clifton Bridge. Although the design predictions were satisfactory, the study showed that using the site measurements of the wind field parameters in the prediction instead of the design values would underestimate the torsional and vertical responses by 40%. Xu and Zhu (2005) studied the dynamic response of the Tsing Ma Bridge in China using the framework proposed by Zhu and Xu (2005), which accounts for skew-winds. Researchers included the bridge towers and cables in their analysis, and their predictions showed reasonable agreement with the field data for the studied 1-hour recording. Wang et al. (2011) used the same framework to conduct time domain analyses for the Runyang Suspension Bridge. The measured and predicted responses were reasonably similar for the single event considered. Wang et al. (2013) compared the buffeting analysis results for the Sutong Bridge that were obtained using the measured and design spectra. Although the agreement between the two responses were excellent, no comparisons were made with the measured response. More recently, Cheynet et al. (2016) studied the buffeting response of the Lysefjord Suspension Bridge in Norway. They compared the measured displacement response with their frequency-domain predictions for one day of continuous measurements. The measured turbulence spectra were used to calculate the response and the results indicated underestimations of the vertical and lateral responses, presumably as a result of the complex topography. The valuable research efforts listed above provide confidence in the existing methods for dynamic response prediction of cable-supported bridges. However, in most of the studies, the response was predicted considering a single event or using limited data. More recordings of strong winds are needed to consider the actual variability in the response. Objective evaluations of the design methodology are not possible if the variability in the measured response is not presented. The sources of discrepancies also remain to be investigated to develop more accurate methods for both predictions and design.

In this study, long-term monitoring data of wind velocity and acceleration from a slender long-span suspension bridge are used to study its dynamic response. The bridge is located in complex terrain in the Norwegian fjords and is subjected to strong winds that are mainly perpendicular to the bridge longitudinal axis. The buffeting response of the bridge is calculated using state-of-the-art methods. The wind turbulence spectra are deduced using design guidelines and also the measured wind characteristics.

The measured acceleration response is compared with the analytical results in the form of buffeting curves.

2. Hardanger Bridge

The Hardanger Bridge (Fig. 1) crosses the Hardangerfjord in Norway and serves as an important link on the highway between the major cities of Oslo and Bergen. Since it opened to the public in 2013 after a four-year construction period, it has stood as the longest suspension bridge in Norway, with a main span of 1310 meters. It is located in a mountainous region (Fig. 2) that is subjected to strong wind storms. Hardanger Bridge supports only two traffic lanes in each direction with an additional lane for bicycles and pedestrians; thus, with its long main span, this bridge constitutes an exceptionally slender and lightweight structure. The bridge girder is a streamlined steel box girder that is 3.2 meters high and 18.3 meters wide. In the design stage, the shape of the girder was governed by wind effects (flutter and vortex shedding); a cross-sectional drawing of the girder is shown in Fig. 3. The bridge was constructed by individually lifting 60-meter long sections that were fastened to the hangers. Transverse bulkheads were added every four meters along the deck and guide vanes were installed underneath the girder to mitigate vortex-induced vibrations. The girder is supported by 130 hangers and 2 main cables, which are located at either side of the girder. The longest hanger is 128 meters long, and the shortest one is 2 meters long; the hanger diameter is 70 mm. Each of the bridge cables consists of 19 strands that are made of 528 galvanized 5.3 mm wires; the cables were assembled by pulling each wire into place using a spinning wheel travelling along the cable path. The two bridge towers are supported by concrete foundations on rock and they reach up to 200 meters. Each tower consists of two massive concrete columns joined by three cross-beams, and the design of the concrete pylons was governed by wind effects in the ultimate limit state.

Fig. 1. Hardanger Bridge (image by the authors)

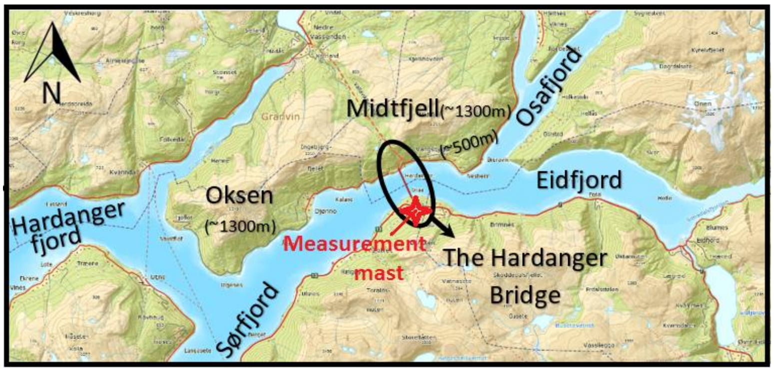

Fig. 2. Local topography around Hardanger Bridge

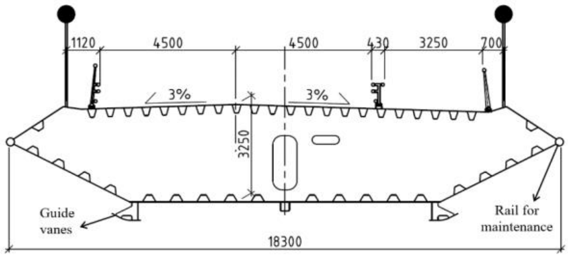

Fig. 3. Scale drawing of the Hardanger Bridge cross-section

3. Design basis for Hardanger Bridge

The Norwegian handbook for bridge design (N400, Statens-Vegvesen 2009) provides regulations for the design of bridge structures, including suspension bridges. This document states that field measurements must be performed if the bridge span is longer than 300 meters and the wind load is significant. According to N400, the along-wind (I_u) and vertical (I_w) turbulence intensities are given as

$$I_u(z) = \frac{c_{tt}}{\ln(z/z_0)}, \quad I_w = 0.5 I_u \tag{1}$$

where c_{tt} is the turbulence factor, z is the height above the ground and z_0 is the roughness length, which can be taken as 0.01 meters, in accordance with the document. The turbulence factor was given as 1.2 for the Hardanger Bridge by the NPRA, which accounts for topographical influences. The above formula gives a turbulence intensity of 11.5% for the along-wind turbulence and 5.7% for the vertical turbulence. To calculate the one-point auto-spectra of the along-wind (S_u) and vertical (S_w) turbulence components, N400 recommends the following expression, which is in the form of the Kaimal spectra (Kaimal et al. 1972):

$$\frac{fS_i}{\sigma_i^2} = \frac{a_i \hat{n}_i}{\left(1+1.5 a_i \hat{n}_i\right)^{5/3}}, \ \hat{n}_i = \frac{f\ {}^{x}L_i(z)}{U(z)}, \ i = u, w \tag{2}$$

where f is the frequency in Hz, U is the mean wind speed, $\sigma_{u,w}$ are the standard deviations of the u and w turbulence components, ${}^{x}L_u(z)$ and ${}^{x}L_w(z)$ denote the longitudinal and vertical length scales, respectively, which are given as functions of height above the ground z. For the Hardanger Bridge deck, ${}^{x}L_u(z)$ and ${}^{x}L_w(z)$ correspond to 171 meters and 14 meters, respectively, at a height of approximately 60 meters above sea level, the spectral parameters are given as a_u = 6.8 and a_w = 9.4. The document adopts Davenport's (1961) expression for the normalized cross-spectrum, which can be written as

$$C(f, \Delta \mathrm{x}) = \exp(-K \frac{f.\Delta \mathrm{x}}{U}) \tag{3}$$

where K is the decay coefficient and Δx is the span-wise separation. The recommended values for the decay coefficients are given as K_u = 10 and K_w = 6.5.

During the design of the Hardanger Bridge, the turbulence spectra given by N400 were refined, using field measurements from a 45-meter-high mast (Harstveit 2007) and wind tunnel tests on a terrain model of the bridge site (Sætran and Malvik 1991); the location of the measurement mast is shown in Fig. 2. The four-year (1988-1992) data from the mast were combined with long-term (1981-2006) data from a nearby lighthouse to obtain the wind characteristics. Considering both the field and wind tunnel measurements data, the N400 recommendations were calibrated by NPRA, to form the design basis for the wind characteristics (Statens-Vegvesen 2006). The turbulence intensities for the along-wind and vertical turbulence were reported as 13.7% and 7%, respectively. The expression given in Eqn. (2) was used to calculate one-point spectra of turbulence, where the length scale values were adjusted to 360 meters for the along-wind component and 21 meters for the vertical component to match the measurements. The following expression was used for the normalized cross-spectra:

$$C_i(f, \Delta x) = \left(1 - \frac{1}{2}\kappa \Delta x\right).\exp(-\kappa \Delta x), \ \ \kappa = b_i \sqrt{\left(\frac{2\pi f}{U}\right)^2 + \left(\frac{1}{c_i\ {}^{x}L_u}\right)^2}, \ \ i = u, w \tag{4}$$

where the coefficients are given as b_u = 1, c_u = 1.5, b_w = 0.5 and c_w = 1. This expression is based on the original formulation by Krenk (1996), and the coefficients were introduced to provide better agreement with the site measurements. This expression is superior to the classical exponential expression for two reasons: it allows for values smaller than unity for large separations at zero frequency, and it allows for negative values. This equation overcomes the theoretical problem of Eqn. (3), which contradicts the zero mean definition of the turbulence component (Holmes 2007; Krenk 1996).

4. Monitoring of Hardanger Bridge

Measurement system

Immediately after Hardanger Bridge opened in 2013, it was instrumented with an extensive monitoring system with the aim of measuring wind velocities and accelerations at several locations along the bridge deck and at the tower tops. The monitoring system consists of 20 triaxial accelerometers and 9 3D anemometers; the sensor layout is given in Fig. 4. The monitoring system consists of 20 triaxial accelerometers and 9 anemometers; the sensor layout is given in Fig. 4. For wind measurements, WindMaster Pro 3-d ultrasonic anemometers form Gill Instruments were used. The wind sensors provide a measurement range of 0-65 m/s, 0.001 m/s resolution and up to 32 Hz data output rate. The accelerometers installed on the bridge are of CUSP-3D series strong motion accelerographs by Canterbury Seismic Instruments. These sensors are robust triaxial accelerometers and are capable of measuring accelerations in ± 4g range with 200 Hz data output rate. Of the accelerometers, 16 are located inside the bridge girder, 14 of which are installed on both ends of the girder as pairs to capture the torsional motion of the girder, and the remaining 4 are fixed inside the two tower tops. Eight of the anemometers are distributed along the bridge span, and they are attached to the hangers 8 meters above the girder to avoid wind flow disturbances due to the deck and traffic. The last anemometer stands on top of the Vallavik (North) tower.

The accelerometer data are sampled at 200 Hz initially, whereas the anemometer data are sampled at 32 Hz. A common sampling frequency of 20 Hz is used for both the accelerometer and anemometer data in this study, so both data were downsampled to 20 Hz prior to use. The wind data were transformed to a coordinate system oriented in the mean wind direction, and its mean and fluctuating parts (turbulence components) were decomposed using a 10-minute averaging interval for the wind characteristics study. The fluctuations in the along-wind direction are denoted as u(t), where the fluctuations in the cross-wind and vertical directions are denoted as v(t) and w(t) turbulence components, respectively. The vertical and lateral accelerations of the bridge girder were calculated by averaging two signals from the accelerometers on each side of the girder; the torsional acceleration was then calculated by dividing the difference between the two signals by the deck width. Since only the wind-induced vibrations of the bridge are of interest, it is desired to exclude vibrations induced by other sources from the data. Looking at the frequency content of the acceleration signals, it is seen that the response is dominated by low frequency vibrations when the wind speed is above 8 m/s. Among the recordings with lower wind speeds, the ones dominated by high frequency vibrations were removed from the data, assuming the traffic-induced vibrations were profound. Moreover, the remaining acceleration data were passed through a low-pass filter with 1 Hz cut-off frequency, since it is expected that wind-induced response of the bridge is in the low frequency (0-1 Hz) range (Brownjohn et al. 1994; Xu and Zhu 2005a). It should also be noted that the traffic density in Hardanger Bridge is usually very low; therefore, large variations in response due to traffic is not likely.

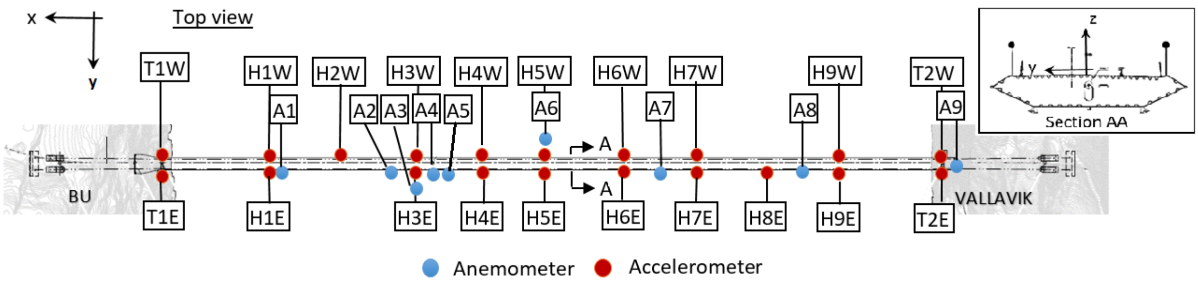

Fig. 4. Sensor layout

Mean wind speed and direction

The monitoring system has been recording data in a discontinuous manner since 2013. The system is triggered if the wind velocity in the horizontal plane exceeds 15 m/s in any of the anemometers. After the system is triggered, the acceleration and wind velocity are recorded for 30 minutes. Occasionally, the system is also triggered manually to also include recordings with low wind speeds in the database., A total of 8530 10-minute recordings from the database are considered in this paper; these data were recorded between December 2013 and September 2016 (a total of 35 months). A threshold wind speed of 3 m/s is used, meaning that recordings with lower wind speeds were discarded and are not presented in this paper. Fig. 5 shows a wind rose plot of the 10-minute mean wind speed on the local topography map of the bridge site. In the figure, the 0° direction corresponds to the longitudinal axis of the bridge.

Mean wind speeds of up to 30 m/s were recorded, and the wind direction was almost perpendicular to the bridge axis. The wind was in general blowing along the fjord due to the steep mountains on either end of the bridge (Fig. 5); however, skew winds with deviations of up to 30° from the perpendicular direction were also measured.

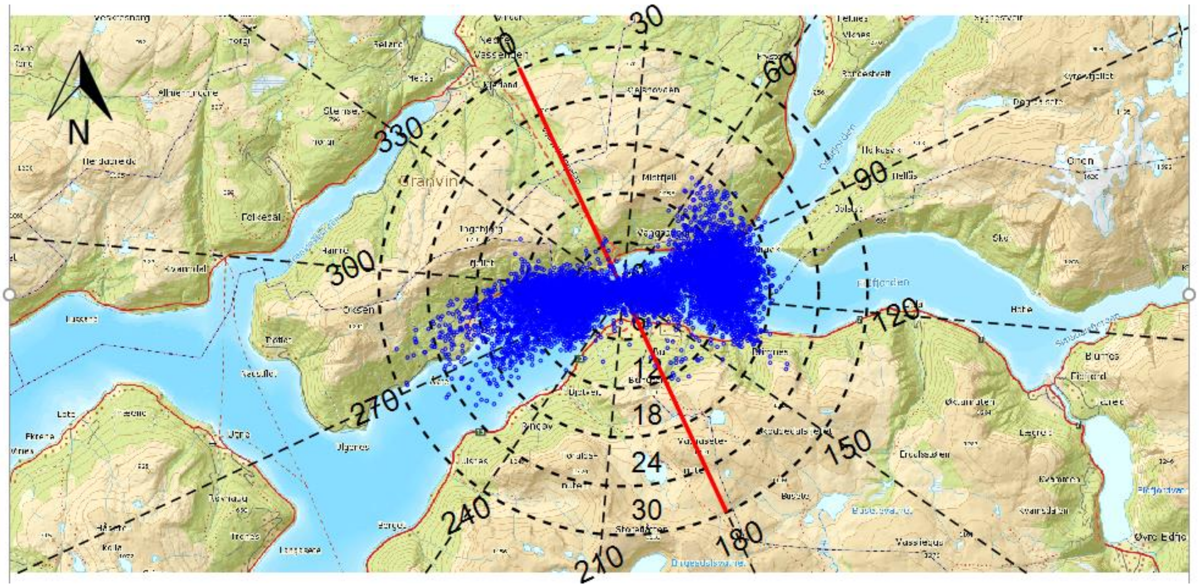

Fig. 5. Wind rose plot of mean wind speed averaged over 10 minutes

Turbulence intensity

The turbulence intensity provides direct information on the turbulent energy of the wind, and is therefore critically important for describing the characteristics of atmospheric turbulence. The along-wind (u) and vertical (w) turbulence intensities were calculated for the 10-minute recordings and were plotted against the mean wind speed (Fig. 6). Fig. 7 shows the probability distribution plots of the along-wind (u) and vertical (w) turbulence intensities. The cross-wind (v) component is assumed to have a negligible influence on bridge dynamic response and is, therefore not presented. Since the turbulence intensity is dependent on the mean wind speed, the data were divided into four segments with different wind speeds. Lognormal distributions were fitted to the data and are shown in the same figures; the plots indicate that lognormal distributions can represent the data fairly well. The probability distribution function of the lognormal distribution is written as

$$f(x \mid \mu,\sigma) = \frac{1}{x\sigma\sqrt{2\pi}} e^{\left\{\frac{-(\ln x-\mu)^2}{2\sigma^2}\right\}}; x > 0 \tag{5}$$

where μ and σ are the parameters of the distribution (the mean and standard deviation of the natural logarithm of the random variable, respectively) and are given in the figures for the fitted distributions. The mean values of the along-wind and vertical turbulence intensities were 16.5% and 7.1%, respectively.

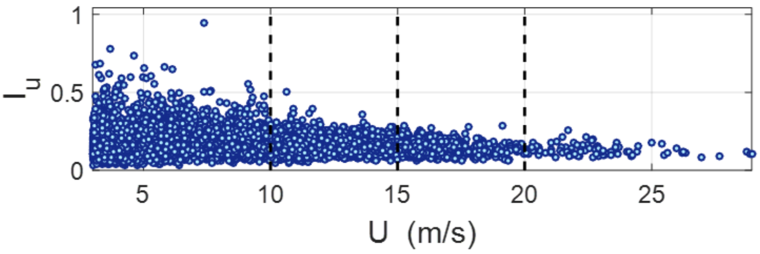

(a)

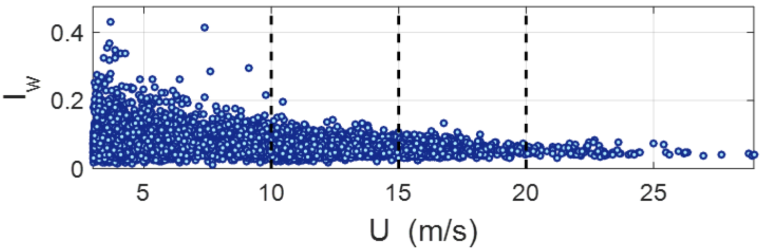

(b)

Fig. 6. Turbulence intensity vs. mean wind speed: (a) u component and (b) w component

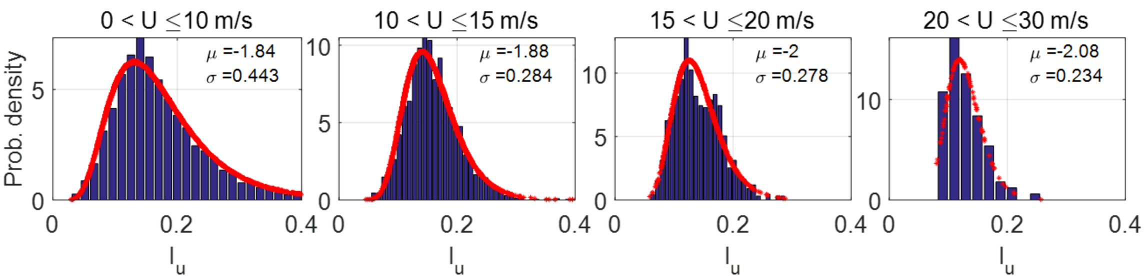

(a)

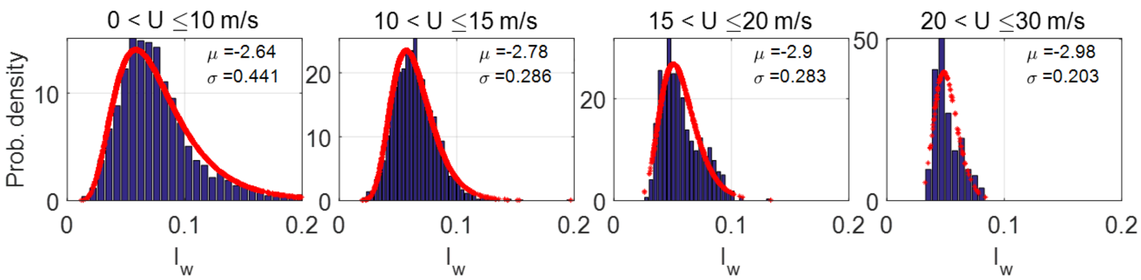

(b)

Fig. 7. Probability distributions of turbulence intensity: (a) along-wind and (b) vertical turbulence.

Angle-of-attack

The angle-of-attack (β) is defined here as the angle between the mean wind velocity vector and the horizontal plane. The aerodynamic properties of the bridge section are affected by the inclination of the mean wind; consequently, the structural response is influenced by the angle-of-attack. The angle-of-attack was calculated using the anemometer data and plotted against the mean wind speed for all recordings, as shown in Fig. 8. This figure indicates that the angle-of-attack exhibits significant variability at low and moderate wind speeds. Large angles were obtained from the recordings with low wind speeds and a nonstationary nature. In general, the mean wind velocity was inclined towards the positive z direction (upwards), and the mean value of the angle-of-attack was 3° for whole velocity range, which is rather substantial. The conditional probability distributions of β are given in Fig. 9 for different velocity ranges along with the normal distribution fits to the data. The angle-of-attack can be approximated as normally distributed, with a mean value of approximately 2°-3°, even for the strong winds.

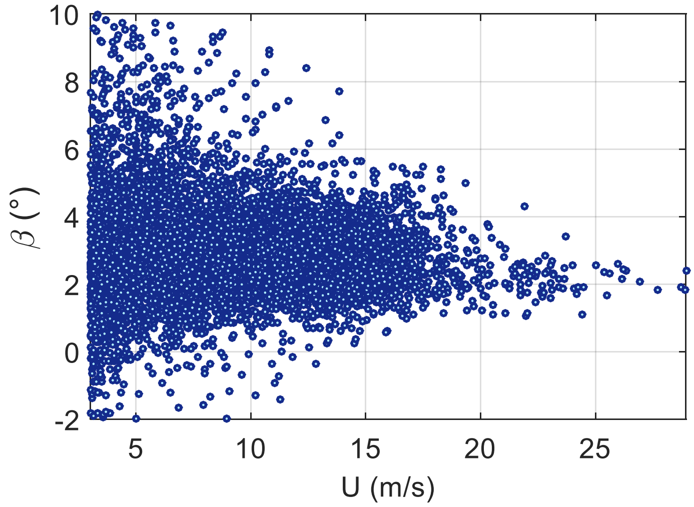

Fig. 8. Angle-of-attack vs. mean wind speed

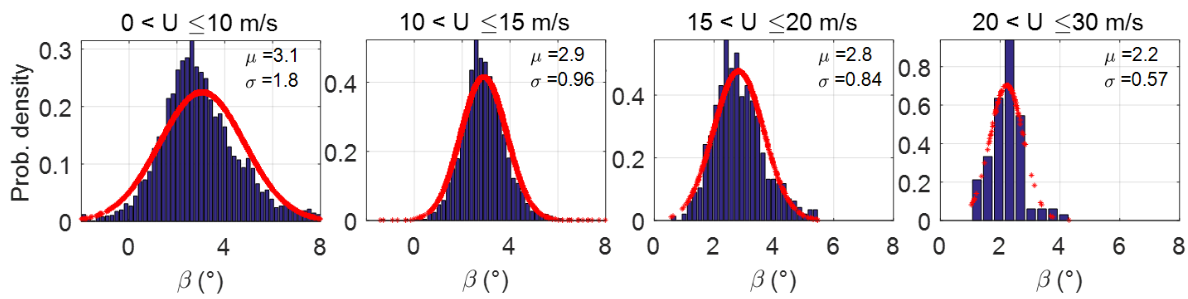

Fig. 9. Probability distributions of the angle-of-attack (β)

One-point spectra of turbulence

The one-point auto-spectra of the along-wind and vertical turbulence components are often used to describe the gust loading on suspension bridges in dynamic response calculations. However, the one-point cross-spectra of u and w components, are often neglected assuming that their effects on the dynamic response are insignificant. Therefore, the auto power spectral densities (PSDs) of the u and w turbulence components were estimated for the entire database. For each 10-minute signal, the spectra were estimated using Welch's averaged periodogram method (Welch 1967). The time series of the turbulence components were divided into 8 segments with 50% overlap; then, the PSDs were calculated using the Fast Fourier Transform (FFT) method and were averaged after applying a Hamming window to each segment. The Welch estimate of the PSD results in high variance; thus, the estimates were smoothed using a parametric least squares fit. The following parametric expression, in the form of the Kaimal spectra, was fitted to each estimate:

$$\frac{S_{u,w} f}{\sigma_{u,w}^{\;2}} = \frac{A_{u,w} f_z}{(1+1.5A_{u,w} f_z)^{5/3}}, \quad f_z = \frac{f\,z}{U} \tag{6}$$

where f is the frequency in Hz, U is the mean wind speed, z is the height above the ground, $S_{u,w}$ are the auto-spectra and $\sigma_{u,w}$ are the standard deviations of the u and w turbulence components. The remaining non-dimensional parameters $A_{u,w}$ are determined by the least squares fit to the measurement data. The resulting probability distributions of the spectral parameters are presented in Fig. 10 along with the fitted lognormal distributions. The data is not divided into velocity intervals, since no strong dependence was observed with the mean wind speed. The corresponding mean values were 18.8 and 2.8 for A_u and A_w, respectively. The parameters of the fitted distributions are indicated on the plots.

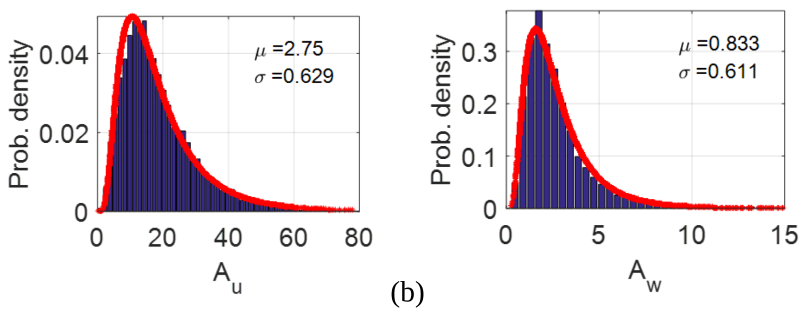

(a) (b)

Fig. 10. Probability distributions of the spectral parameters: (a) u component and (b) w component

Normalized cross-spectra

A complete description of the atmospheric turbulence and consequently the gust loading on any line-like structure requires spatial correlation information of the turbulence components in addition to the one-point statistics. This is commonly achieved using normalized cross-spectra. The normalized cross-spectrum can be interpreted as a frequency-dependent correlation coefficient and is defined as (Dyrbye and Hansen 1997)

$$C_{nm}(f,\Delta x) = \frac{S_{nm}(f)}{\sqrt{S_n(f)S_m(f)}} \tag{7}$$

where, S_{nm} $n \in \{u,w\}$, $m \in \{u,w\}$ denotes the cross-spectral density while S_n $n \in \{u,w\}$ and S_m $m \in \{u,w\}$ denote the auto-spectral densities at two points separated by a distance Δx. The complex part of the cross-spectral density contains the phase information, which is regarded as small for separations transverse to the wind flow and is often neglected in practice. The normalized cross-spectra for the 10-minute recordings were calculated using the Welch spectral density estimates and neglecting the complex part of the cross-spectra. The normalized cross-spectra are usually represented by the simple exponential expression proposed by Davenport (1961), the expression of which is given in Eqn. (3). The decay coefficients $K_{u,w}$ can be estimated using a least squares approximation of the data. Despite its weaknesses at low frequencies and large separation distances (Simiu and Scanlan 1996), Davenport's expression approximates the actual normalized cross-spectra reasonably well and is frequently used in practice. The expression was fitted to the measurement data in least squares sense and the decay coefficients were obtained for all recordings. Four sensor pairs were used to estimate the root coherences from the database; the corresponding separation distances were 20, 40, 80 and 210 meters for the four sensor pairs. The curve fitting of the root coherence function is shown in Fig. 11 for a 10-minute recording as an example. The resulting probability distributions of the decay coefficients are presented in Fig. 12 for the u and w components along with the corresponding lognormal distributions that were fitted to the data. The mean values of the decay coefficients were 7.63 for the along-wind component and 7.78 for the vertical component. This expression causes difficulties when the correlation is not apparent; thus, any K value above 20 is considered non-coherent and is not included in the probability distribution.

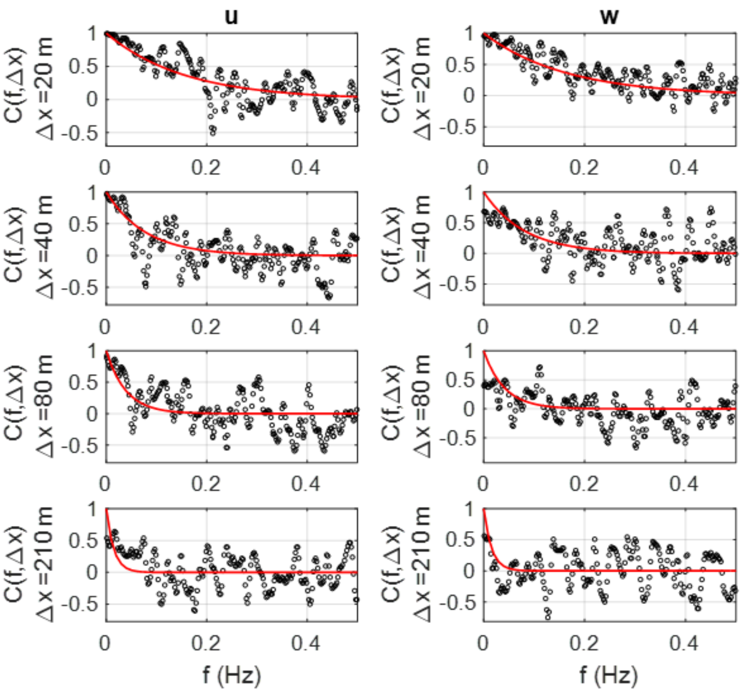

Fig. 11. Estimation of the decay coefficients using least squares fitting for a sample 10-minute recording (K_u = *6.55*, K_w = *6.31*). The histograms represent the measured data and the curves were fitted using Eqn. (3).

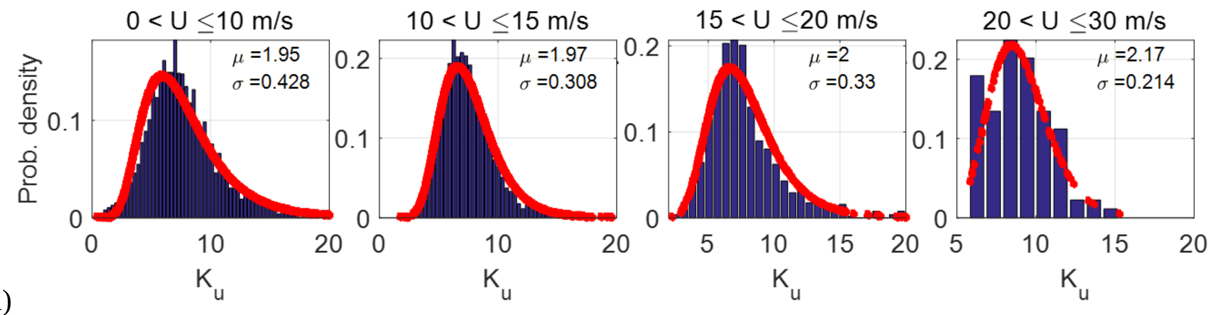

(a)

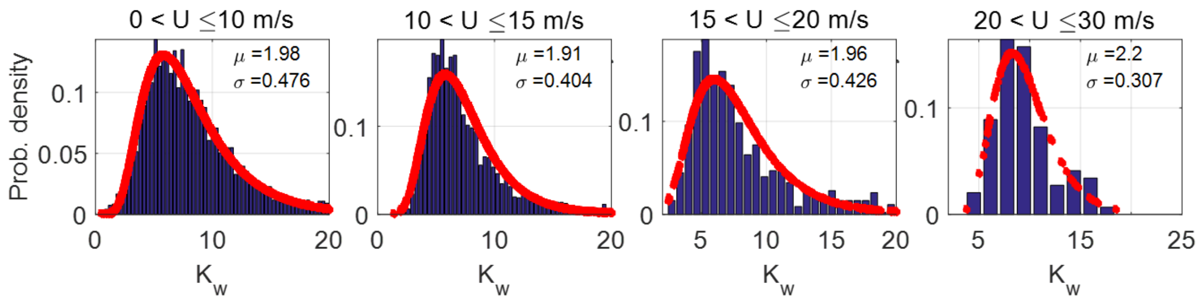

(b)

Fig. 12. Probability distributions of the decay coefficients: (a) u component and (b) w component

5. Buffeting analysis in frequency domain

Buffeting analysis method

The buffeting response of Hardanger Bridge was calculated in frequency domain using the classical multimode theory (Chen et al. 2001; Jain et al. 1996). The analytical procedure is briefly introduced here; more detailed formulations can be found elsewhere (Katsuchi et al. 1998; Øiseth et al. 2010). The analysis is based on the solution of the fully coupled system of equations of motion, where the bridge displacements are represented in generalized coordinates of the mode shapes in still-air. The multimode system of equations of motion including the aeroelastic effects is written in frequency domain as

$$\tilde{\mathbf{M}}_0\mathbf{G}_{\ddot{\eta}}(\omega)+(\tilde{\mathbf{C}}_0-\tilde{\mathbf{C}}_{ae}(U,\omega))\mathbf{G}_{\dot{\eta}}(\omega)+(\tilde{\mathbf{K}}_0-\tilde{\mathbf{K}}_{ae}(U,\omega))\mathbf{G}_{\eta}(\omega)=\mathbf{G}_{\mathbf{Q}_{buff}}(\omega) \tag{8}$$

where ω is the circular frequency, $\tilde{\mathbf{M}}_0$, $\tilde{\mathbf{K}}_0$ and $\tilde{\mathbf{C}}_0$ are the generalized mass, stiffness and damping matrices in still-air, respectively, $\tilde{\mathbf{C}}_{ae}$ and $\tilde{\mathbf{K}}_{ae}$ are the generalized aeroelastic damping and stiffness matrices respectively, $\mathbf{G}_{\ddot{\eta}}$, $\mathbf{G}_{\dot{\eta}}$ and $\mathbf{G}_{\eta}$ denote the Fourier transforms of the acceleration, velocity and displacement responses in generalized coordinates, respectively, and $\mathbf{G}_{\mathbf{Q}_{buff}}$ denotes the generalized buffeting force. According to random vibration theory (Wirsching et al. 2006), the PSD matrices of the generalized displacement response ($\tilde{\mathbf{S}}_R(\omega)$) and the buffeting force ($\mathbf{S}_{\mathbf{Q}_{buff}}(\omega)$) are related as follows:

$$\begin{gathered}\tilde{\mathbf{S}}_R(\omega)=\left[\mathbf{E}_{\eta}^{-1}(\omega)\mathbf{S}_{\mathbf{Q}_{buff}}(\omega)\mathbf{E}_{\eta}^{-1*}(\omega)\right]\\ \mathbf{E}_{\eta}(U,\omega)=\left[-\tilde{\mathbf{M}}_0\omega^2+(\tilde{\mathbf{C}}_0-\tilde{\mathbf{C}}_{ae}(U,\omega))i\omega+(\tilde{\mathbf{K}}_0-\tilde{\mathbf{K}}_{ae}(U,\omega))\right]\end{gathered} \tag{9}$$

The frequency-dependent modal aeroelastic stiffness and damping matrices can be obtained by

$$\begin{gathered}\tilde{\boldsymbol{K}}_{ae}(U,\omega)=\int_L(\boldsymbol{\Phi}^T\boldsymbol{K}_{ae}(U,\omega)\,\boldsymbol{\Phi})dx\\ \tilde{\boldsymbol{C}}_{ae}(U,\omega)=\int_L(\boldsymbol{\Phi}^T\boldsymbol{C}_{ae}(U,\omega)\,\boldsymbol{\Phi})dx\end{gathered} \tag{10}$$

where

$$\mathbf{K}_{ae}=\frac{\rho B^2}{2}\omega^2\begin{bmatrix}P_4^* & P_6^* & BP_3^*\\ H_6^* & H_4^* & BH_3^*\\ BA_6^* & BA_4^* & B^2A_3^*\end{bmatrix},\ \ \mathbf{C}_{ae}=\frac{\rho B^2}{2}\omega\begin{bmatrix}P_1^* & P_5^* & BP_2^*\\ H_5^* & H_1^* & BH_2^*\\ BA_5^* & BA_1^* & B^2A_2^*\end{bmatrix} \tag{11}$$

In the above expressions, $\boldsymbol{\varphi}_i = \left[\phi_y, \phi_z, \phi_\theta\right]^T$ is the mode shape vector, $\boldsymbol{\Phi}$ denotes the matrix of the mode shapes, $P_{1,2,..,6}^*$, $H_{1,2,..,6}^*$, $A_{1,2,..,6}^*$ denote the dimensionless aerodynamic derivatives, B is the width of the girder and ρ is the air density. Having established the system matrices, the buffeting action needs to be defined. The elements of the spectral matrix of the buffeting force can be written in generalized coordinates as

$$\begin{gathered} \mathbf{S}_{Q_{buff}}(\omega) = \int_L \int_L \boldsymbol{\Phi}^T(x_1)\mathbf{B}_q(\omega)\mathbf{S}_V(\Delta x, \omega)\mathbf{B}_q^T(\omega)\boldsymbol{\Phi}(x_2)dx_1 dx_2 \\ \mathbf{S}_V(\Delta x, \omega) = \begin{bmatrix} S_{uu}(\Delta x, \omega) & S_{uw}(\Delta x, \omega) \\ S_{uw}(\Delta x, \omega) & S_{ww}(\Delta x, \omega) \end{bmatrix} \end{gathered} \tag{12}$$

where $\mathbf{S}_V(\Delta x, \omega)$ is the cross-spectral density matrix containing the auto and cross-spectral densities of the turbulence components at the two points x_1 and x_2, which are separated by a distance of Δx. The matrix $\mathbf{B}_q(\omega)$ includes the steady-state force coefficients:

$$\mathbf{B}_q(\omega) = \frac{\rho U B}{2} \begin{bmatrix} 2(D/B)\bar{C}_D & ((D/B)C'_D - \bar{C}_L) \\ 2\bar{C}_L & (C'_L + (D/B)\bar{C}_D) \\ 2B\bar{C}_M & BC'_M \end{bmatrix} \tag{13}$$

Here, $\bar{C}_D$, $\bar{C}_L$ and $\bar{C}_M$ are the mean values of the steady-state force coefficients associated with the drag, lift and moment, respectively, C'_D, C'_L and C'_M are the corresponding derivatives, and D denotes the girder height. The steady-state force coefficients were obtained from the wind tunnel tests by Hansen et al. (2006) and are given in Table 1. The aerodynamic admittance functions are taken as unity throughout the study due to lack experimental data, which is expected to yield conservative results (Bietry et al. 1995; Larose and Mann 1998; Macdonald 2003). Finally, the root mean square (RMS) acceleration response can be obtained from the displacement spectra using

$$\sigma_R = \sqrt{\int_0^\infty S_{\ddot{R}}(\omega)d\omega}, \quad S_{\ddot{R}}(\omega) = \omega^4 \left[\boldsymbol{\Phi}(x)\tilde{\mathbf{S}}_R(\omega)\boldsymbol{\Phi}^T(x)\right] \tag{14}$$

where $S_{\ddot{R}}(\omega)$ and $S_R(\omega)$ are the acceleration and displacement spectra in global coordinates, respectively.

Table 1. Steady-state force coefficients for the Hardanger Bridge section (Hansen et al. 2006)

$\bar{C}_D$	C'_D	$\bar{C}_L$	C'_L	$\bar{C}_M$	C'_M
0.7	0	-0.25	2.4	0.01	0.74

4.2 Modal analysis

An eigenvalue analysis was performed to obtain the still-air vibration frequencies and mode shapes of Hardanger Bridge, to be used in the buffeting calculations. The FE model of the bridge, which was originally constructed by the NPRA in ABAQUS (Dassault Systèmes Simulia et al. 2013), was used in the analysis. The FE model is shown in Fig. 13. The first 100 natural frequencies and the corresponding mode shapes were obtained by solving the classical eigenvalue problem, after the application of dead loads, accounting for the geometric stiffness utilized by the cables. The first 20 modes and the corresponding natural frequencies and periods are listed in Table 2 along with the dominant nature of each mode; some of the mode shapes are illustrated in Fig. 14.

Table 2. First 20 vibration modes of Hardanger Bridge

Mode	Frequency (Hz)	Period (seconds)	Description of the dominant motion
1	0.05	20.00	Symmetric lateral vibration of the deck
2	0.098	10.20	Asymmetric lateral vibration of the deck
3	0.11	9.09	Asymmetric vertical vibration of the deck
4	0.14	7.14	Symmetric vertical vibration of the deck
5	0.169	5.92	Symmetric lateral vibration of the deck
6	0.197	5.08	Symmetric vertical vibration of the deck
7	0.21	4.76	Asymmetric vertical vibration of the deck
8	0.225	4.44	Symmetric lateral vibration of the cables
9	0.232	4.31	Asymmetric lateral vibration of the cables
10	0.233	4.29	Asymmetric lateral vibration of the deck and the cables
11	0.244	4.10	Symmetric lateral vibration of the deck and the cables
12	0.272	3.68	Symmetric vertical vibration of the deck
13	0.293	3.41	Asymmetric lateral vibration of the deck
14	0.33	3.03	Asymmetric vertical vibration of the deck
15	0.36	2.78	Symmetric torsional vibration of the deck
16	0.373	2.68	Symmetric lateral vibration of the cables
17	0.392	2.55	Symm. lateral vibration of the deck accompanied by torsion
18	0.394	2.54	Symmetric vertical vibration of the deck
19	0.406	2.46	Asymmetric lateral vibration of the deck and the cables
20	0.407	2.46	Asymmetric lateral vibration of the cables

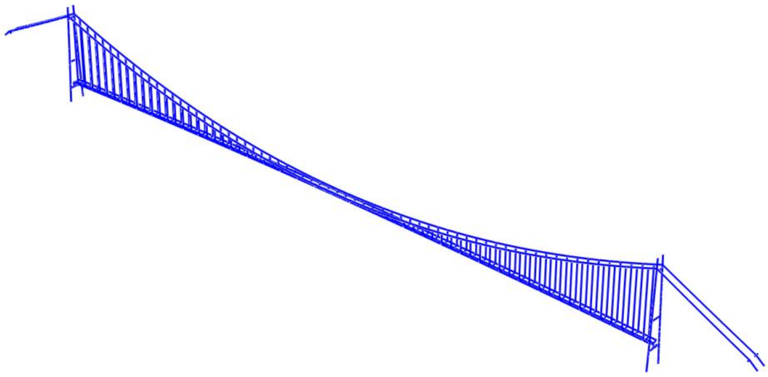

Fig. 13. FE model of Hardanger Bridge

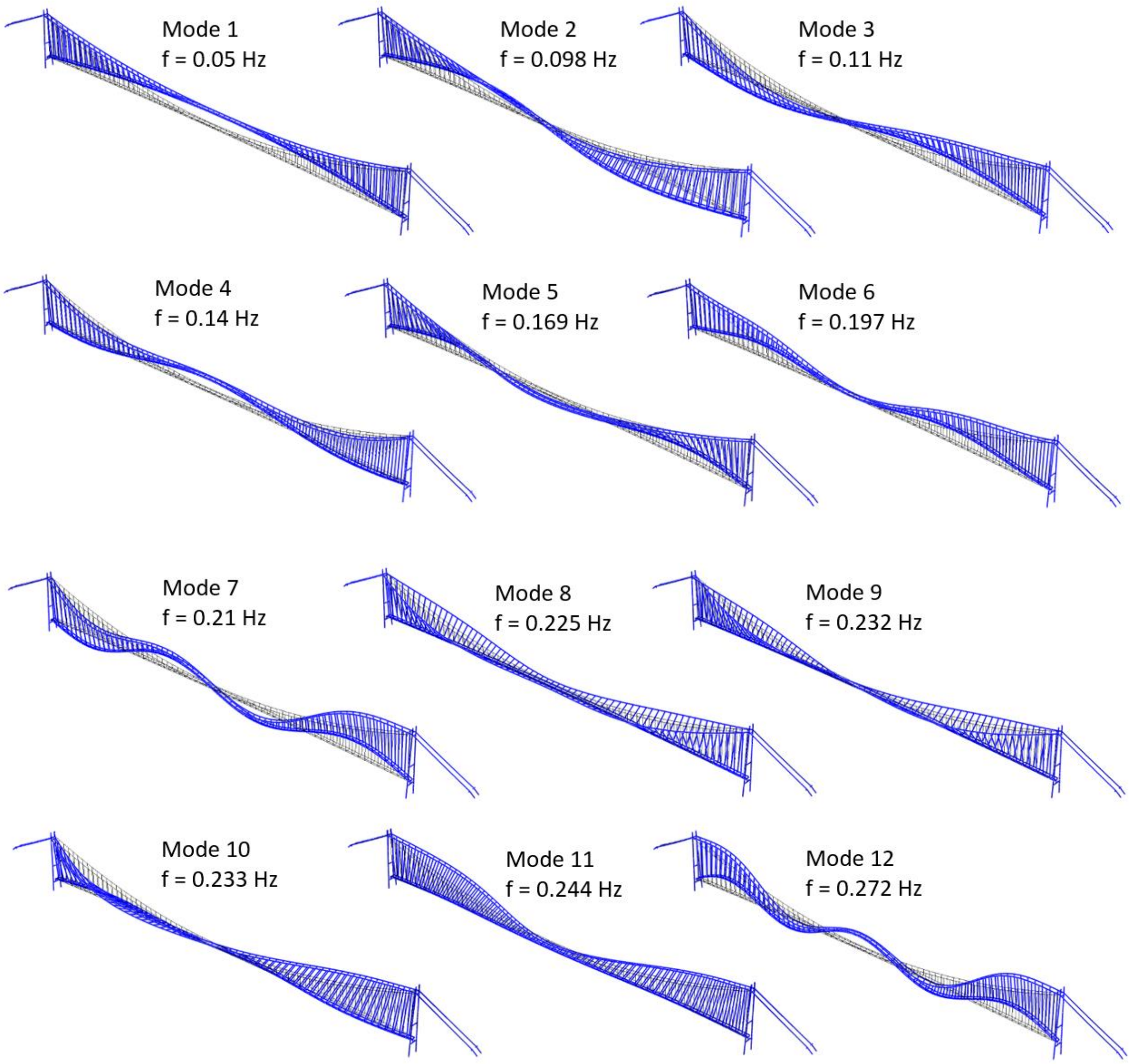

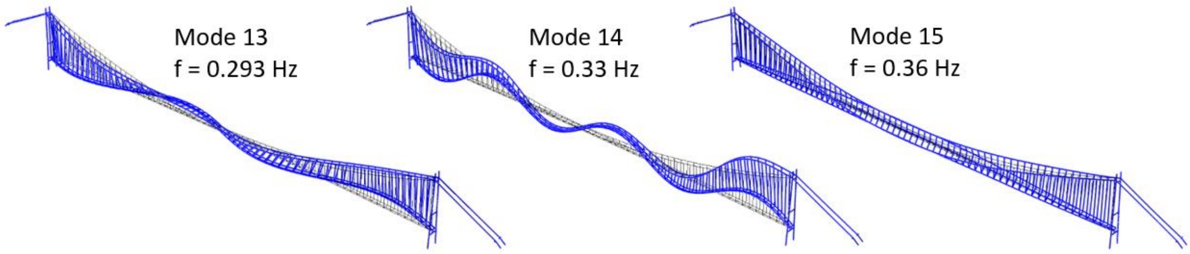

Fig. 14. Mode shapes of Hardanger Bridge for the first 15 vibration modes

Wind turbulence spectra

The wind turbulence spectral matrix (S_v in Eqn. (12)), must be established to calculate the buffeting response. Four different spectral matrices are described here to be used in the response analyses. The first two spectral matrices were calculated according to N400 guidelines and the design basis for Hardanger Bridge, the expressions for which are given in Section 2. Then, as a third case, the probability distributions of the turbulence parameters were used to calculate the turbulence spectra. The spectral parameters $A_{u,w}$ and the decay coefficients $K_{u,w}$ were taken as the 50th percentile values from the fitted lognormal distributions considering the whole wind speed range. Due to their strong dependence on the wind speed (Fig. 6), the turbulence intensities were taken as the 50th percentile values from the conditional probability distributions for different wind speed segments (Fig. 7). For the fourth case, instead of the 50th percentile values, the 5th percentile values for the decay coefficients and the 95th percentile values for the turbulence intensities were used to calculate the spectral density matrix; the spectral parameter was the same as in the third case. For both the third and the fourth cases, the auto-spectra and the normalized cross-spectra were calculated using Eqns. (3) and (6). The cross-spectra of the u and w components were neglected in all cases. Throughout the rest of the paper, the four cases listed above are referred to as the 'N400', 'design', 'modified design' and 'conservative' spectra, respectively.

For comparison, the corresponding parameters given in Eqns. (3) and (6) were calculated for the N400 guidelines and for the design basis; the resulting parameters corresponding to each spectra are presented in Table 3. The auto-spectral densities and the normalized cross-spectra for the u and w components are presented in Fig. 15 and Fig. 16 using the parameters given in Table 3 and a mean wind speed of 16 m/s.

Table 3. Parameters for the spectral density and normalized cross-spectra of turbulence from Eqns. (6) & (3)

	A_u	A_w	K_u	K_w	I_u	I_w
N400	19.4	2.2	10	6.5	0.113	0.057
Design	40.8	3.3	8.8	6.3	0.136	0.068
Modified design						
$0 < U \leq 10$	15.7	2.3	7.14	7.06	0.159	0.071
$10 < U \leq 15$	15.7	2.3	7.14	7.06	0.153	0.062
$15 < U \leq 20$	15.7	2.3	7.14	7.06	0.136	0.055
$20 < U \leq 30$	15.7	2.3	7.14	7.06	0.125	0.051
Conservative						
$0 < U \leq 10$	15.7	2.3	3.84	3.39	0.33	0.15
$10 < U \leq 15$	15.7	2.3	3.84	3.39	0.244	0.099
$15 < U \leq 20$	15.7	2.3	3.84	3.39	0.214	0.087
$20 < U \leq 30$	15.7	2.3	3.84	3.39	0.184	0.071

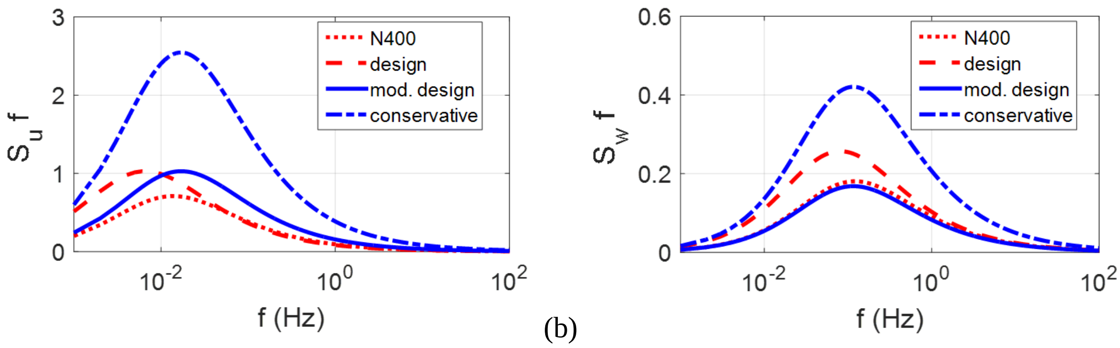

(a) (b)

Fig. 15. One-point spectra of turbulence (U = 16 m/s): (a) u component and (b) w component

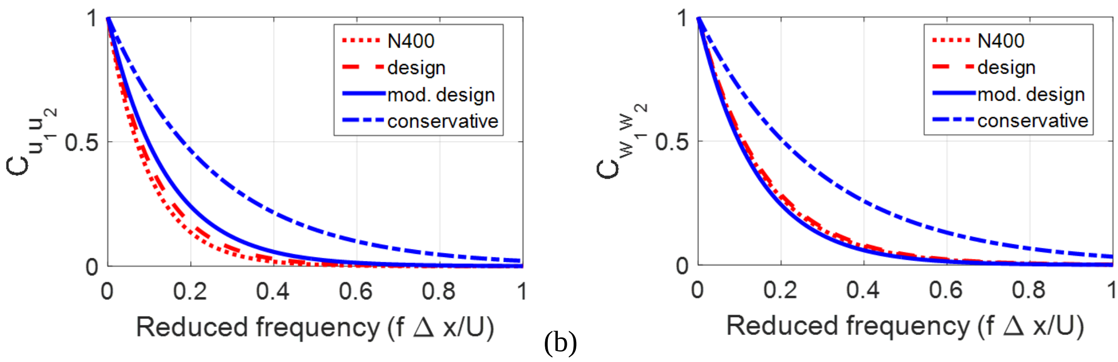

(a) (b)

Fig. 16. Normalized cross-spectra of turbulence (U = 16 m/s): (a) u component and (b) w component

Self-excited forces

Motion-dependent self-excited forces were included in the analysis using the aeroelastic stiffness and damping matrices given in Eqns. (10) and (11). These matrices consist of frequency dependent aerodynamic derivatives, which are distinct properties of the bridge section that are obtained experimentally. The aerodynamic derivatives were obtained by Siedziako et al. (2017) from recent forced vibration wind tunnel tests on a section model of Hardanger Bridge. The experimental results are shown in Fig. 17 and Fig. 18 along with rational function approximations using a nonlinear least squares fit to obtain the 18 aerodynamic derivatives as continuous functions of reduced velocity. Here, it should be noted that the aerodynamic derivatives are sensitive to the curve fit where there is no experimental data points. This is the case for the torsional motion, where the interested reduced velocity range (0-0.7) is quite low. Therefore, the curve fit of the derivative A_2 is forced to stay negative in that range to avoid negative damping in the buffeting analysis.

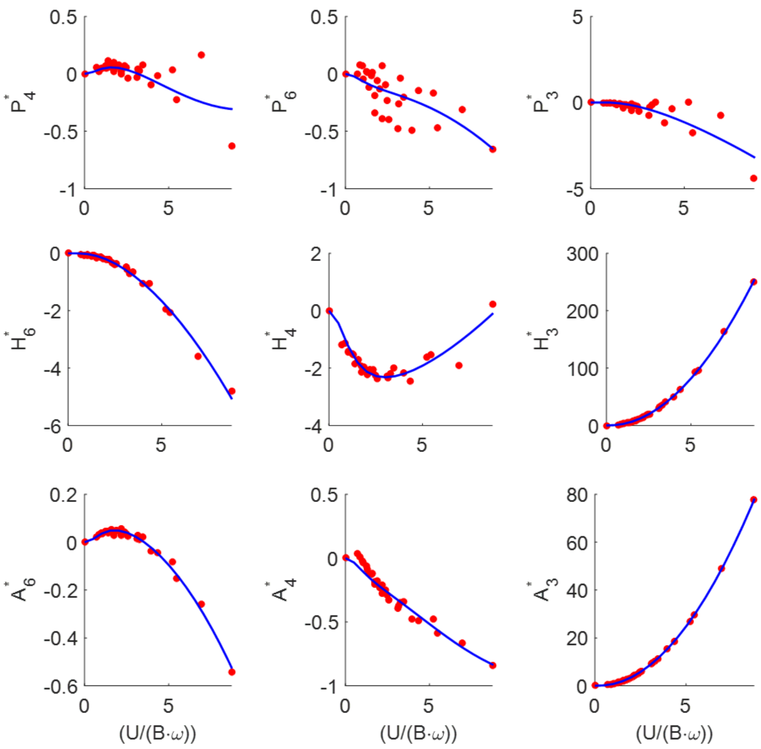

Fig. 17. Aerodynamic derivatives associated with stiffness. (The dots represent experimental data and the continuous curves represent the curve fit)

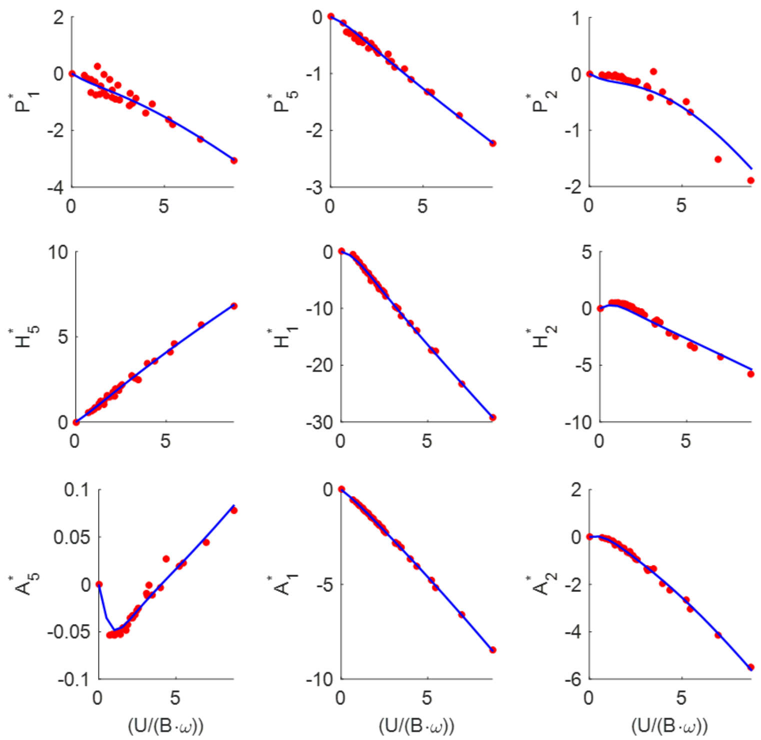

Fig. 18. Aerodynamic derivatives associated with damping. (The dots represent experimental data and the continuous curves represent the curve fit)

6. Acceleration response at the midspan

The standard deviations of the zero-mean turbulence components were obtained directly from the 10-minute long time series of the lateral, vertical and torsional accelerations. The resulting root-mean square (RMS) responses at the midspan are presented in Fig. 19 against the mean wind speed. Here, due to the large number of data points and remarkable variability in the data, it is deemed important to elaborate on how the scatter is distributed. For this purpose, the data points in the figures are color coded to highlight the relative density of the data. The relative density corresponding to each data point was calculated by dividing the plotting area into rectangular regions using a fine orthogonal grid. Then the relative density corresponding to each data point was multiplied with the square of the mean wind speed (U^2) to give more weight to the data with higher wind speeds. This helps visualizing the distribution of scatter in response for a given wind velocity. Furthermore, histograms of response components are also given in figures for narrow velocity intervals. It is seen that the response data is in general log-normally distributed, resembling the wind field statistics. The torsional response was plotted for the easterly and the westerly winds separately due to an apparent distinction observed in two responses. The distinction mainly arises from the differences in the upwind terrain of the two wind directions. The vertical turbulence intensity of the easterly winds are in general much higher than the westerly winds especially for the winds approaching from 60-100° direction range, due to the disturbance of the wind flow by the mountains. It is observed that the distribution of scatter deviates from the lognormal distribution around wind speeds of 15 m/s and this is more profound in the case of easterly winds. A least-squares polynomial fit to the data is also shown in the figures to highlight the mean of the scatter.

The scatter observed in the plots are mainly due to terrain effects; however, many other factors contribute to the variability. Nonstationary features in turbulent fluctuations, which is commonly observed in such complex terrain can alter the wind characteristics (Chen et al. 2007; Tao et al. 2016; Wang et al. 2016) and result into variations in the dynamic response. The effect of such features are studied analytically by Chen (2015) and Hu et al. (2013, 2017). Although it is seen that non-stationarity of the wind imposes variations on the response, such variations are small compared to the variability of the wind characteristics and the response of the Hardanger Bridge. For reasonably high wind speeds (U > 8 m/s), rapid changes in mean wind speed or direction are not observed when an averaging interval of 10 minutes is used. Therefore, the traditional stationary wind model was adopted in the present study, mostly due to its common use in practice.

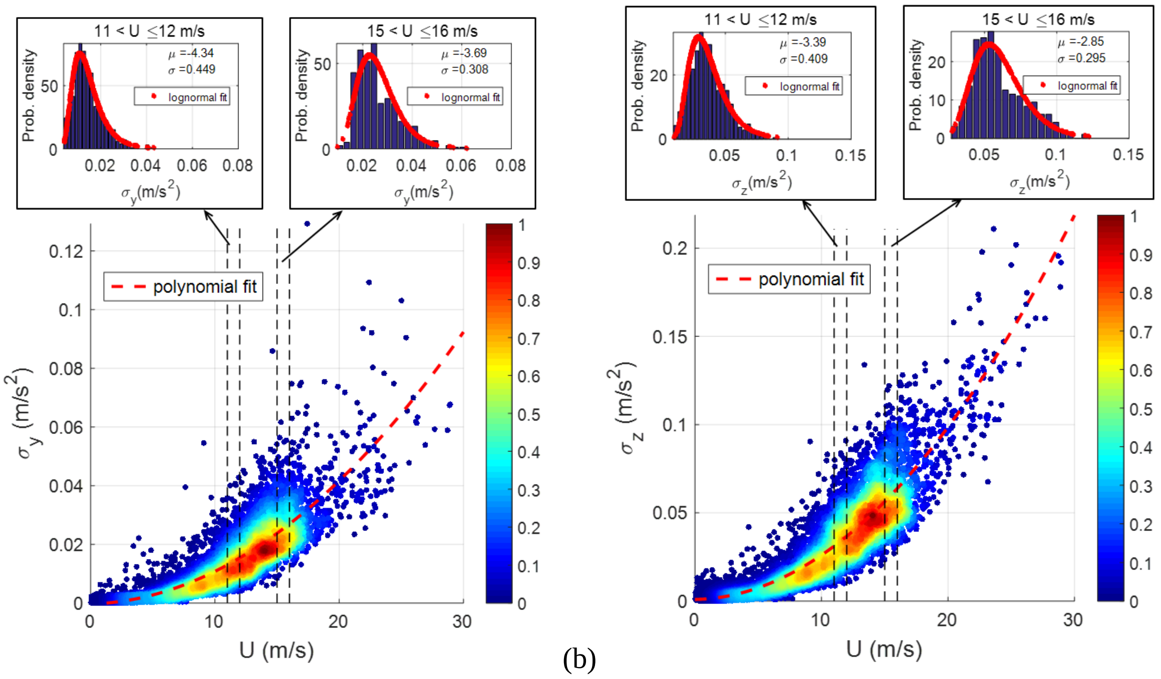

(a) (b)

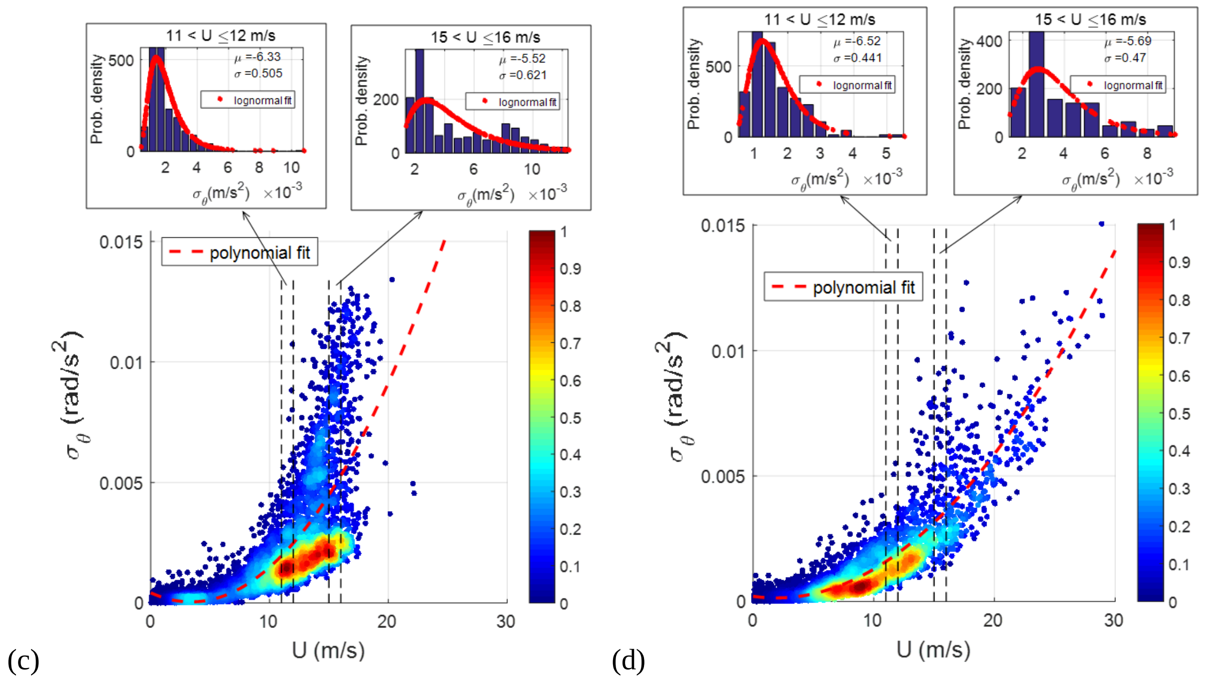

Fig. 19. RMS acceleration response at the midspan (color bar indicates the data density): (a) lateral response, (b) vertical response, (c) torsional response for easterly winds, (d) torsional response for westerly winds

7. Comparison of the acceleration response

The RMS acceleration response of Hardanger Bridge was calculated using the procedure described in section 4.1. The first 100 mode shapes of the structure (0.05 – 1.6 Hz) are included in the analysis and the RMS accelerations are obtained by numerically integrating the acceleration response spectra. In general, the lateral response is dominated by a large peak at the first fundamental mode (0.05 Hz), where significant contributions from higher modes can be observed in case of the vertical and torsional modes. A damping ratio of 0.5% was assumed for the structural damping in the calculations and utilized for all the participated modes. The damping ratio is selected based on the recommendation of N400, which suggests the use of a damping ratio between 0.5 and 0.8% for steel structures. If a lower damping ratio such as 3% is used in the analysis with the design method, 15%, 9% and 28% increase is observed under 30 m/s mean wind in the lateral, vertical and torsional RMS responses, respectively with the design method. On the other hand, the use of a higher damping ratio of 1% resulted into 20%, 14% and 29% decrease in the lateral, vertical and torsional RMS responses, respectively. It is observed that the torsional response is the most sensitive to the structural damping because of the low aerodynamic damping in torsional motion; however, such high variations in structural damping ratio are unrealistic. The acceleration responses were evaluated for the four different turbulence spectra described in Section 5, and the resulting response prediction approaches are named after the corresponding spectra, i.e., 'N400', 'design', 'modified design' and 'conservative'. For the modified design and conservative approaches, the steady-state force coefficients were modified according to the mean angle-of-attack of 3°, which was obtained from the measurements in full-scale. The modified steady-state force coefficients were obtained from the wind tunnel tests of Hansen et al. (2006), as listed in Table 4.

Table 4. Steady-state force coefficients for the Hardanger Bridge section for an angle-of-attack of 3° (Hansen et al. 2006)

$\bar{C}_D$	C'_D	$\bar{C}_L$	C'_L	$\bar{C}_M$	C'_M
0.815	0	-0.112	2.5	0.036	0.86

RMS acceleration responses for the four analytical cases and the experimental data are shown in Fig. 20 and Fig. 21: Fig. 20 shows the acceleration response at the midspan (accelerometer pair H5E & H5W), whereas Fig. 21 shows the acceleration response at approximately the quarter-span (accelerometer pair H3E & H3W), which is 240 meters away (towards the south end) from the midspan. The results yield very similar response levels at both points for all analytical cases and the field data, so a common discussion is valid for both the midspan and quarter-span responses. For all response components, the N400 method underestimated the measured response; this was somewhat improved when the design values were used. The modified design approach resulted into similar curves as the design approach. Compared to the design predictions, the vertical and torsional response predictions were slightly higher for the low wind speeds and slightly lower for the high wind speeds, whereas the lateral response predictions were similar. As expected, the conservative approach gave the highest response predictions. Moreover, using the conditional probability distributions avoided severe overestimation of the response at high wind speeds. The 'conservative' approach provided the most satisfactory results as candidate curves for design of such structures. This observation indicates that the wind-related variables are not independent from each other and depend strongly on the mean wind speed. Consequently, better estimations can be obtained by considering the joint interactions of these parameters.

The analytical procedure gave systematically lower lateral response predictions compared to the measured response regardless of the adopted approach. The wind forces acting on the hangers and cables, which are expected to contribute to the lateral response, are neglected in the analyses. This was preferred due to the lack of information on the wind characteristics at the cable level; however, the degree of underestimation imposed is still of interest. In previous analytical studies, Xu et al. (2000) reported a 15% increase in lateral displacement response of Tsing Ma Bridge and Zhang (2007) reported a 20% increase for the Runyang Suspension Bridge. For the Hardanger Bridge, the drag force on one cable is around 32% of the force on the bridge deck. Considering the loading on both cables, if the analysis is repeated with a modified drag coefficient of 1.14 for the bridge deck (instead of 0.7), approximately 25% increase is obtained in the lateral response. Although this approach gives a maximum bound for the increase in response due to the cable forces, it is overly conservative since it assumes perfect correlation of wind forces at the cables and at the deck. Moreover, several researchers reported that the span-wise correlation of the wind buffeting forces is stronger than that of the wind turbulence (Jakobsen 1997; Larose and Mann 1998; Yan et al. 2016), which might partly explain the discrepancy.

To investigate the relative importance of the aerodynamic damping on different response components, the analysis with the design method is repeated neglecting the aerodynamic damping. The lateral and the vertical responses increased by 45% and 98% under a mean wind speed of 30 m/s, respectively. The change in torsional response was however very small; only a 0.5% increase was observed, indicating that the aerodynamic damping utilized by the use of aerodynamic derivatives was small for the torsional motion.

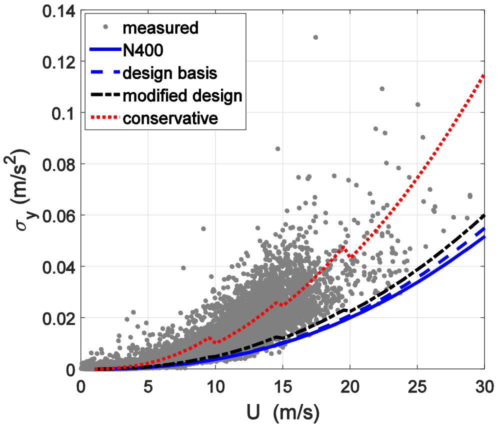

(a)

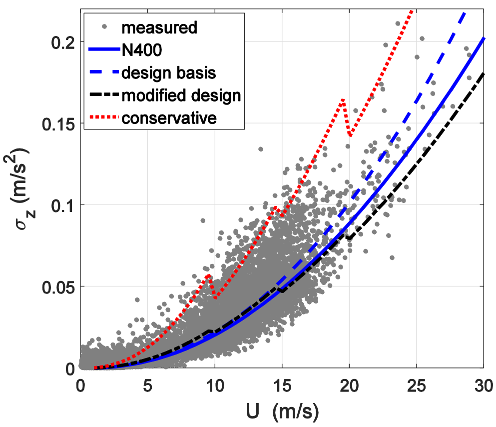

(b)

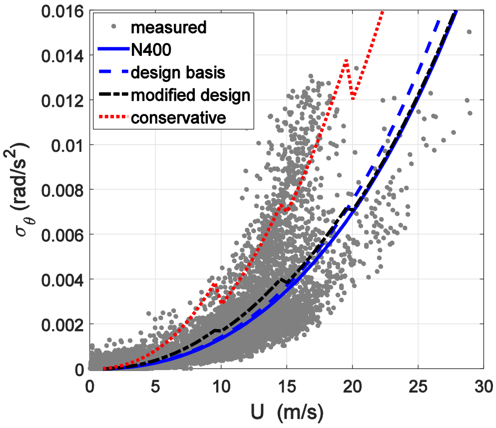

(c)

Fig. 20. Comparison of the RMS acceleration response at the midspan (a) lateral acceleration, (b) vertical acceleration and (c) torsional acceleration

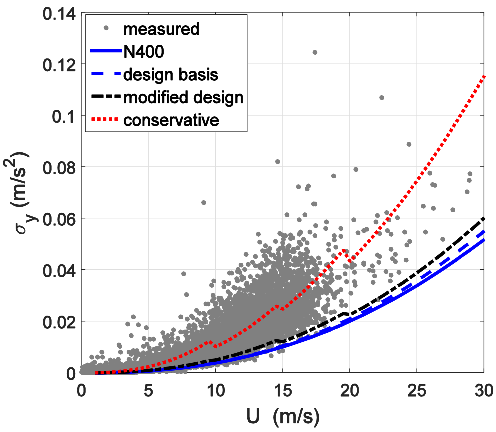

(a)

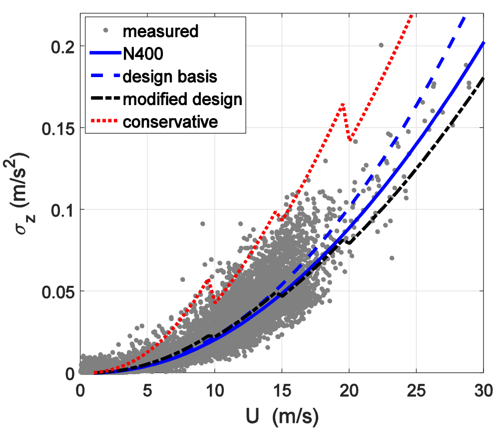

(b)

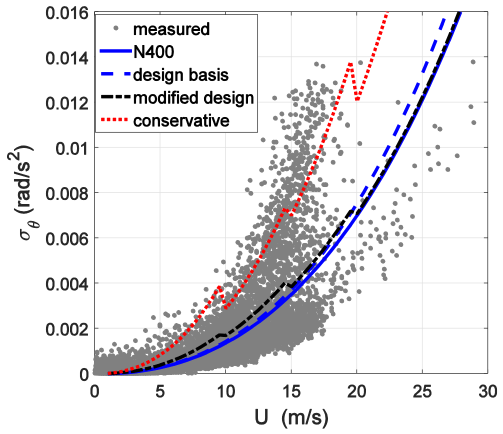

(c)

Fig. 21. Comparison of the RMS acceleration response at the quarter-span (at x = 240 m) (a) lateral acceleration, (b) vertical acceleration and (c) torsional acceleration

8. Conclusions

The long-term monitoring data of wind velocity and acceleration from Hardanger Bridge were used to study the wind characteristics and to compare the acceleration response with analytical predictions. The dynamic wind-induced response of the bridge was evaluated in frequency domain, using the design spectrum and several modified design spectra. Comparing the results led to the following conclusions for the specific case of Hardanger Bridge:

- The design curve underestimated the measured response. The design basis calibrated using field measurements gave slightly better estimations compared to directly using the N400 recommendations.
- Using the 50th percentile values of the wind field parameters from the long-term monitoring data improved the predictions; however, the resulting curves were still not considered satisfactory design curves due to the scatter in the field data.
- The wind forces on the cables are thought to contribute to the dynamic response of the bridge, especially for the lateral vibration response. More sophisticated analyses that include the cables and hangers are necessary to account for such effects on the overall response prediction.
- A conservative approach that used 95th or 5th percentile values of the wind field parameters from the monitoring data provided more desirable design curves. Overestimating the response

at high wind speeds was avoided by using conditional probability distributions for the turbulence intensities.

- The results imply that the wind field variability should be considered in the buffeting response analysis of such structures. Furthermore, the interactions among the wind field parameters should be considered, preferably using joint probability distributions or conditional probability distributions.

9. Acknowledgments

The research described in this paper was financially supported by the Norwegian Public Roads Administration.

10. REFERENCES

Bietry, J., Delaunay, D., and Conti, E. (1995). “Comparison of full-scale measurement and computation of wind effects on a cable-stayed bridge.” *Journal of Wind Engineering and Industrial Aerodynamics*, 57(2–3), 225–235.

Brownjohn, J. M. W., Bocciolone, M., Curami, A., Falco, M., and Zasso, A. (1994). “Humber bridge full-scale measurement campaigns 1990-1991.” *Journal of Wind Engineering and Industrial Aerodynamics*, 52(C), 185–218.

Caetano, E., Cunha, A., Moutinho, C., and Magalhães, F. (2015). “Dynamic characterization and continuous dynamic monitoring of long span bridges.” *International Conference on Multi-Span Large Bridges*, CRC Press/Balkema, Porto, Portugal, 771–780.

Caracoglia, L., and Jones, N. P. (2003). “Time domain vs. frequency domain characterization of aeroelastic forces for bridge deck sections.” *Journal of Wind Engineering and Industrial Aerodynamics*, 91(3), 371–402.

Chen, J., Hui, M. C. H., and Xu, Y. L. (2007). “A comparative study of stationary and non-stationary wind models using field measurements.” *Boundary-Layer Meteorology*, 122(1), 105–121.

Chen, X. (2015). “Analysis of multimode coupled buffeting response of long-span bridges to nonstationary winds with force parameters from stationary wind.” *Journal of Structural Engineering (United States)*, 141(4), 1–14.

Chen, X., and Kareem, A. (2001). “Nonlinear response analysis of long-span bridges under turbulent winds.” *Journal of Wind Engineering and Industrial Aerodynamics*, 89(14–15), 1335–1350.

Chen, X., Kareem, A., and Matsumoto, M. (2001). “Multimode coupled flutter and buffeting analysis of long span bridges.” *Journal of Wind Engineering and Industrial Aerodynamics*, 89(7–8), 649–664.

Chen, X., Matsumoto, M., and Kareem, A. (2000). “Time Domain Flutter and Buffeting Response Analysis of Bridges.” *Journal of Engineering Mechanics*, 126(1), 7–16.

Cheynet, E., Jakobsen, J. B., and Snæbjörnsson, J. (2016). “Buffeting response of a suspension bridge in complex terrain.” *Engineering Structures*, 128, 474–487.

Costa, C., Borri, C., Flamand, O., and Grillaud, G. (2007). “Time-domain buffeting simulations for wind-bridge interaction.” *Journal of Wind Engineering and Industrial Aerodynamics*, 95(9–11), 991–1006.

Cross, E. J., Koo, K. Y., Brownjohn, J. M. W., and Worden, K. (2013). “Long-term monitoring and data analysis of the Tamar Bridge.” *Mechanical Systems and Signal Processing*, 35(1–2), 16–34.

Dassault Systèmes Simulia, Fallis, A. ., and Techniques, D. (2013). “ABAQUS documentation.” *Abaqus 6.12*.

Davenport, A. G. (1961). “The spectrum of horizontal gustiness near the ground in high winds.” *Quarterly Journal of the Royal Meteorological Society*, 87(372), 194–211.

Davenport, A. G. (1962). “Buffeting of a suspension bridge by storm winds.” *Journal of structural Division*, 88(3), 233–268.

Dyrbye, C., and Hansen, S. (1997). *Wind Loads on Structures*. Wiley.

Hansen, S., Lollesgaard, M., Rex, S., Jacobsen, J., and Hansen, E. (2006). *The Hardanger Bridge: Static and Dynamic Wind Tunnel Tests with A Section Model*. Copenhagen.

Harstveit, K. (2007). *Hardanger Bridge: characteristics of strong wind*. Oslo.

Holmes, J. (2007). *Wind Loading on Structures*. Taylor&Francis, New york.

Hu, L., Xu, Y.-L., and Huang, W.-F. (2013). “Typhoon-induced non-stationary buffeting response of long-span bridges in complex terrain.” *Engineering Structures*, 57(0), 406–415.

Hu, L., Xu, Y.-L., Zhu, Q., Guo, A., and Kareem, A. (2017). “Tropical Storm–Induced Buffeting

Response of Long-Span Bridges: Enhanced Nonstationary Buffeting Force Model." *Journal of Structural Engineering*.

Hui, M. C. H., Larsen, A., and Xiang, H. F. (2009). "Wind turbulence characteristics study at the Stonecutters Bridge site: Part II: Wind power spectra, integral length scales and coherences." *Journal of Wind Engineering and Industrial Aerodynamics*, 97(1), 48–59.

Jain, A., Jones, N. P., and Scanlan, R. H. (1996). "Coupled Flutter and Buffeting Analysis of Long-Span Bridges." *Journal of Structural Engineering*, 122(7), 716–725.

Jakobsen, J. B. (1997). "Span-wise structure of lift and overturning moment on a motionless bridge girder." *Journal of Wind Engineering and Industrial Aerodynamics*, 69–71, 795–805.

Kaimal, J. C. J., Wyngaard, J. C. J., Izumi, Y., Coté, O. R., and Cote, O. R. (1972). "Spectral Characteristics of Surface-Layer Turbulence." *Quarterly Journal of the …*, 98(417), 563–589.

Katsuchi, H., Jones, N. P., Scanlan, R. H., and Akiyama, H. (1998). "Multi-mode flutter and buffeting analysis of the Akashi-Kaikyo bridge." *Journal of Wind Engineering and Industrial Aerodynamics*, 77–78, 431–441.

Krenk, S. (1996). "Wind Field Coherence And Dynamic Wind Forces." *IUTAM Symposium on Advances in Nonlinear Stochastic Mechanics: Proceedings of the IUTAM Symposium held in Trondheim, Norway, 3--7 July 1995*, A. Naess and S. Krenk, eds., Springer Netherlands, Dordrecht, 269–278.

Larose, G. L., and Mann, J. (1998). "Gust loading on streamlined bridge decks." *Journal of Fluids and Structures*, 12(5), 511–536.

Larsen, A., and Larose, G. L. (2015). "Dynamic wind effects on suspension and cable-stayed bridges." *Journal of Sound and Vibration*, Academic Press, 334(1), 2–28.

Macdonald, J. H. G. (2003). "Evaluation of buffeting predictions of a cable-stayed bridge from full-scale measurements." *Journal of Wind Engineering and Industrial Aerodynamics*, 91(12–15), 1465–1483.

Miyata, T. (2003). "Historical view of long-span bridge aerodynamics." *Journal of Wind Engineering and Industrial Aerodynamics*, 91(12–15), 1393–1410.

Miyata, T., Yamada, H., Katsuchi, H., and Kitagawa, M. (2002). "Full-scale measurement of Akashi-

Kaikyo Bridge during typhoon." *Journal of Wind Engineering and Industrial Aerodynamics*, 90(12–15), 1517–1527.

Øiseth, O., Rönnquist, A., and Sigbjörnsson, R. (2012). "Finite element formulation of the self-excited forces for time-domain assessment of wind-induced dynamic response and flutter stability limit of cable-supported bridges." *Finite Elements in Analysis and Design*, 50, 173–183.

Øiseth, O., Rönnquist, A., and Sigbjørnsson, R. (2010). "Simplified prediction of wind-induced response and stability limit of slender long-span suspension bridges, based on modified quasi-steady theory: A case study." *Journal of Wind Engineering and Industrial Aerodynamics*, 98(12), 730–741.

Sætran, L. R., and Malvik, I. M. (1991). *Hardanger Bridge - Wind characteristics study on a terrain model in the wind tunnel*. Trondheim.

Scanlan, R. H. (1978). "The action of flexible bridges under wind, II: Buffeting theory." *Journal of Sound and Vibration*, 60(2), 187–199.

Scanlan, R. H., and Tomko, J. J. (1971). "Airfoil and Bridges Deck Flutter Derivatives." *Journal of the Engineering Mechanics Division (ASCE)*, 97, 1717–1737.

Siedziako, B., Øiseth, O., and Rönnquist, A. (2017). "An enhanced forced vibration rig for wind tunnel testing of bridge deck section models in arbitrary motion." *Journal of Wind Engineering and Industrial Aerodynamics*, in press.

Simiu, E., and Scanlan, R. H. (1996). *Winds Effects on Structures: Fundamentals and Applications to Design*. Wiley.

Statens-Vegvesen. (2006). *The Hardanger Bridge design basis - wind characteristics*.

Statens-Vegvesen. (2009). *N400 Handbook for bridge design*.

Tao, T., Wang, H., and Wu, T. (2016). "Comparative Study of the Wind Characteristics of a Strong Wind Event Based on Stationary and Nonstationary Models." *Journal of Structural Engineering*.

Wang, H., Hu, R., Xie, J., Tong, T., and Li, A. (2013). "Comparative study on buffeting performance of sutong bridge based on design and measured spectrum." *Journal of Bridge Engineering*, 18(7), 587–600.

Wang, H., Li, A., and Hu, R. (2011). "Comparison of Ambient Vibration Response of the Runyang

Suspension Bridge under Skew Winds with Time-Domain Numerical Predictions." *Journal of Bridge Engineering*, 16(4), 513.

Wang, H., Wu, T., Tao, T., Li, A., and Kareem, A. (2016). "Measurements and analysis of non-stationary wind characteristics at Sutong Bridge in Typhoon Damrey." *Journal of Wind Engineering and Industrial Aerodynamics*, 151, 100–106.

Welch, P. D. (1967). "The Use of Fast Fourier Transform for the Estimation of Power Spectra: A Method Based on Time Averaging Over Short, Modified Periodograms." *IEEE Transactions on Audio and Electroacoustics*, 15(2), 70–73.

Wirsching, P. H., Paez, T. L., and Ortiz, K. (2006). *Random Vibrations: Theory and Practice*. Dover Publications.

Xu, Y.-L. (2013). *Wind Effects on Cable-Supported Bridges*. John Wiley & Sons.

Xu, Y. L., Sun, D. K., Ko, J. M., and Lin, J. H. (2000). "Fully coupled buffeting analysis of Tsing Ma suspension bridge." *Journal of Wind Engineering and Industrial Aerodynamics*, 85(1), 97–117.

Xu, Y. L., and Zhu, L. D. (2005a). "Buffeting response of long-span cable-supported bridges under skew winds. Part 2: Case study." *Journal of Sound and Vibration*, 281(3–5), 675–697.

Xu, Y. L., and Zhu, L. D. (2005b). "Buffeting response of long-span cable-supported bridges under skew winds. Part 2: case study." *Journal of Sound and Vibration*, Academic Press, 281(3–5), 675–697.

Yan, L., Zhu, L. D., and Flay, R. G. J. (2016). "Span-wise correlation of wind-induced fluctuating forces on a motionless flat-box bridge deck." *Journal of Wind Engineering and Industrial Aerodynamics*, 156, 115–128.

Zhang, X. (2007). "Influence of some factors on the aerodynamic behavior of long-span suspension bridges." *Journal of Wind Engineering and Industrial Aerodynamics*, 95(3), 149–164.

Zhu, L. D., and Xu, Y. L. (2005). "Buffeting response of long-span cable-supported bridges under skew winds . Part 1 : theory." *Journal of Sound and Vibration*, 281(3–5), 647–673.